SOFT ROBOTICS
Volume 2, Number 2, 2015

DOI: 10.1089/soro.2014.0023

SoRo
Soft Robotics

ORIGINAL ARTICLE

Pouch Motors: Printable Soft Actuators Integrated with Computational Design

Ryuma Niiyama,[1] Xu Sun,[2] Cynthia Sung,[3] Byoungkwon An,[3] Daniela Rus,[4] and Sangbae Kim[2]

Abstract

We propose pouch motors, a new family of printable soft actuators integrated with computational design. The pouch motor consists of one or more inflatable gas-tight bladders made of sheet materials. This printable actuator is designed and fabricated in a planar fashion. It allows both easy prototyping and mass fabrication of affordable robotic systems. We provide theoretical models of the actuators compared with the experimental data. The measured maximum stroke and tension of the linear pouch motor are up to 28% and 100 N, respectively. The measured maximum range of motion and torque of the angular pouch motor are up to 80° and 0.2 N, respectively. We also develop an algorithm that automatically generates the patterns of the pouches and their fluidic channels. A custom-built fabrication machine streamlines the automated process from design to fabrication. We demonstrate a computer-generated life-sized hand that can hold a foam ball and perform gestures with 12 pouch motors, which can be fabricated in 15 min.

Introduction

Accelerating the design and manufacturing of physical systems from ideas is one of the main challenges in robotics. Manufacturing conventional robotic platforms requires rather complex processes to assemble constituent components: frame, sensors, actuators, and electronics. Expensive components and complex assembly processes drive up the cost of robotic systems and limit commercialization opportunities. The goal of this research is to design and fabricate robotic systems by print technologies, which will shift the paradigm of robot development.[1] An integrated fabrication method for making robots allows both professionals and nonprofessionals to design and fabricate affordable customized robotic systems.

Automating robot fabrication from design to assembly is important for reducing prototyping costs. Recent advancements in three-dimensional (3D) printing technologies allow for affordable rapid prototyping of arbitrary structures with plastic, metal, and rubber. Although such technology drastically expedites prototyping processes, the available materials for 3D printing are still limited and cannot yet replace unique anisotropic raw material properties. An early approach to integrated fabrication is shape deposition manufacturing (SDM) applied in robotics.[2,3] The SDM integrates actuators, sensors, and linkage mechanisms encapsulated in the process of casting structural materials without fasteners. Another approach for facilitating the integration of robotic components is to combine multiple layers of planar sheets and create a 3D robot by folding. Folding laser-machined composite laminates can create links and joints.[4,5] Self-folding origami techniques[6] can automate the folding process of lightweight structures. The reconfigurable modular robot[7] and programmable structures[8,9] are also approaches that can potentially provide a customized robotic system with minimum assembly processes.

New fabrication techniques have been developed for printable components such as instant circuits,[10] printable batteries,[11] and printable optics.[12] These rapid prototyping technologies minimize assembly time and achieve a monolithic system that integrates multiple components.

Although these techniques facilitate the development of printable robotic systems, developing techniques to print actuators has been a challenging task. This is because typically the fabrication of an actuator requires integrating multiple

[1]Department of Mechano-Informatics, School of Information Science and Technology, University of Tokyo, Tokyo, Japan.
[2]Department of Mechanical Engineering and [3]CSAIL, Massachusetts Institute of Technology, Cambridge, Massachusetts.
[4]Autodesk Research, San Francisco, California.

materials in rather complex geometries. For example, to generate electromagnetic force, highly conductive materials are combined with materials with special magnetic properties in complex 3D shapes. Compared with electromagnetic actuation, electrostatic actuation requires fewer special materials and a less complex fabrication process,[13] although the electrostatic actuator requires a substantially large-surface-area device and a high-voltage power supply to generate workable force.

Thermally responsive materials such as shape memory alloys and shape memory polymers also are candidates for simple actuation methods.[8,14,15] However, the temperature control has low bandwidth and limited energy efficiency, and most of them are not reliable over multiple cycles.

Fluidic actuation offers the benefit of simplicity. Pneumatically driven elastomer (specifically, silicone rubber) is a widely used soft robotics technique.[16] This actuation method uses volume expansion of very soft materials such as silicone rubber by pressure modulation. Fiber-reinforced materials and elastomer composites[17] are employed for selective deformation.

Microfluidic actuators have been explored in the field of microelectromechanical systems (MEMS) using various fabrication techniques.[18] Specifically, a membrane actuator called microballoon actuator is used for microrobotics.[19,20] Because the microactuators rely on MEMS-specific materials and fabrication techniques such as etching, lithography, and spin coating, the output force/moment are neither scalable nor usable by robots beyond the millimeter scale. Moreover, in the microballoon actuator, the considerable elastic deformation of the microballoon makes theoretical analysis difficult.[21]

Pneumatic artificial muscle (PAM) actuator, a type of fluidic actuator, is a candidate printable actuator. Unlike hydraulic or pneumatic cylinders, PAM has no sliding components and has inherent compliance and structural flexibility. McKibben-type PAM consists of a few components: an elastic tube, a braided sleeve, and end fittings. Although PAM results in other improved structures,[22,23] it has a bulky cylindrical shapes.

In this article, we introduce the ''pouch motor,'' a new printable actuator that allows automated design and fabrication for affordable robotic applications. We chose fluidic actuators for their structural simplicity and ease of fabrication. This work is an extension of a previous publication.[24] The two-dimensional (2D) design of the actuator is suitable for seamless connection with existing design tools. We developed a customized algorithm to compute robotic designs with pouch motors. In contrast with recent progress in flat PAM[25] that is based on mold casting silicone rubber, we focused on significantly simplified dry manufacturing process combined with automated computational design.

This article contributes by providing planar pneumatic actuators that can be integrated with printable robot systems. First of all, we investigate the theoretical model of the actuator with measurement data. Our contribution also includes both computer-controlled fabrication and automated design algorithm for robotic applications. We develop two practical fabrication methods for the planar actuator: heat stamping and heat drawing. We apply automated design to the actuators and demonstrate on the printable robot hand.

The remainder of this article is structured as follows: In the section Pouch Motors Characterization, we describe a basic concept of the proposed soft actuators and a design workflow for the printable robotic system. Then, we discuss a theoretical model of the actuator supported by experimental results. In the Fabrication Methods section, we describe fabrication methods to implement the actuators based on heat drawing and heat stamping method. In the section Automated Design with Pouch Motors and the section Robotic Applications, we demonstrate an algorithm to automatically generate a 2D design for a robotic system driven by these planar actuators. We conclude the work with a summary of contributions and future work in the Conclusions section.

Pouch Motors Characterization

Design workflow

The design process for a printable pouch motor robot is shown in Figure 1. The user provides the position of the joints and connectors as well as the shape of the robot. Upon user input, the system generates 2D patterns of the actuator, texture, and structure layers. This 2D form factor enables computer-aided design and simplifies fabrication. Each layer, including the actuator layer, is printable by planar fabrication tools. The actuator layer is a group of pouch motors and fluidic channels printed on a duplex thermoplastic film. The texture layer is a colored pattern printed on paper by inkjet/laser printer. The structure layer is a scaffold of the actuator made of stiff material such as paper, fiberboard, and plastics. All the layers

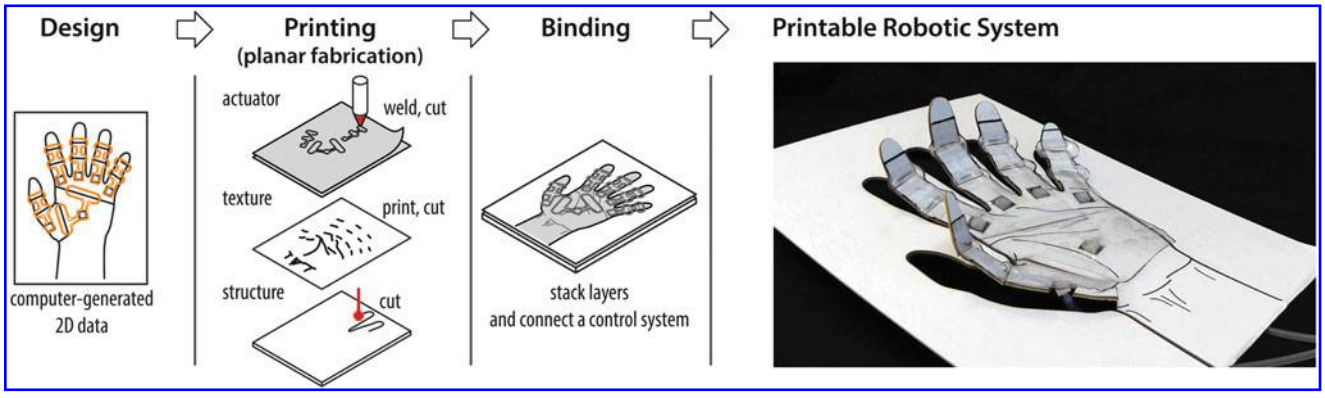

FIG. 1. Overview of the design process for the printable robots with pouch motors. Based on the user input, our system generates the full design of a pouch motor network. The image on the right is an example of a robotic application: a planar life-sized robotic hand popping out from a cardboard. Color images available online at www.liebertpub.com/soro

require cutting process by laser cutter or cutting plotter. Finally, the layers are combined in alignment with double-sided adhesive film/tape or glue. After connecting a control system and initiating a self-folding process, the robot is operable.

Basic function

Pouch motors convert the mechanical work of fluid, such as air, water, and oil, into the deformation of inflatable planar pouches. Changes in length and in curvature are used for the linear (translational) pouch motor and the angular (rotational) pouch motor, respectively (Fig. 2). Stiff output tabs are attached to the edges of the pouch to deliver mechanical power.

The pouches are fabricated by bonding two gas-tight sheets. We chose a heat bonding method that is available for thermoplastics, in terms of performance and manufacturing time. Two heat bonding methods are developed: heat stamping and heat drawing.

Theoretical model of the pouch

We developed a mathematical model of the pouch motor. We focus on two types of joint actuation using the inflatable pouch: linear contraction and angular rotation (Fig. 3). The hinged angular pouch motor is mechanically stable but has smaller range of motion than the angular pouch motor without a hinge.

The initial state of the pouch with no pressure is a flat square, and the geometry of the pouch under positive pressure P is an airfoil shape with cylindrical surfaces on the top and the bottom (Fig. 4a). The pouch on the hinged structure has a cylindrical surface only on the one side (Fig. 4b). As V_h, the volume of the pouch V, increases, the radius of the curvature r of the cylindrical surfaces decreases. We assume that the membrane of the pouch has zero bending stiffness and is inextensible. Thus, we assume that there is no elastic energy

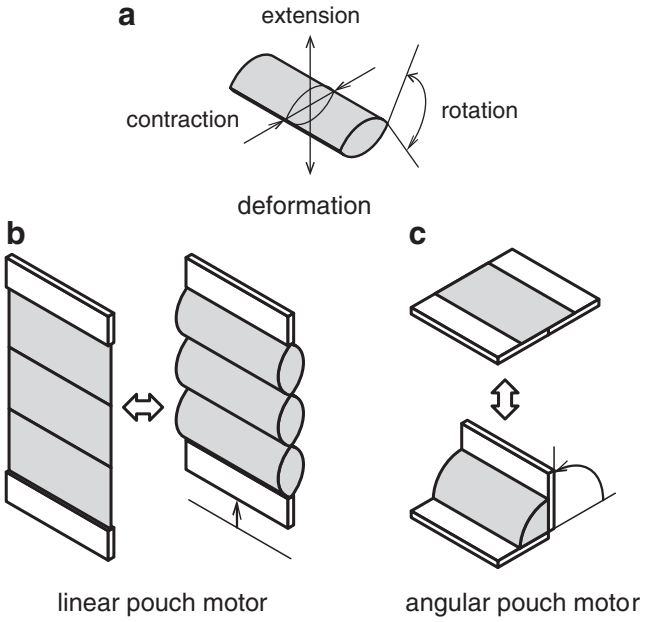

FIG. 2. **(a)** Possible dimension change of a pouch. Modes of motions actuated by pouch motors can be **(b)** linear or **(c)** angular. The gray and white parts indicate inflatable pouches and stiff structure, respectively.

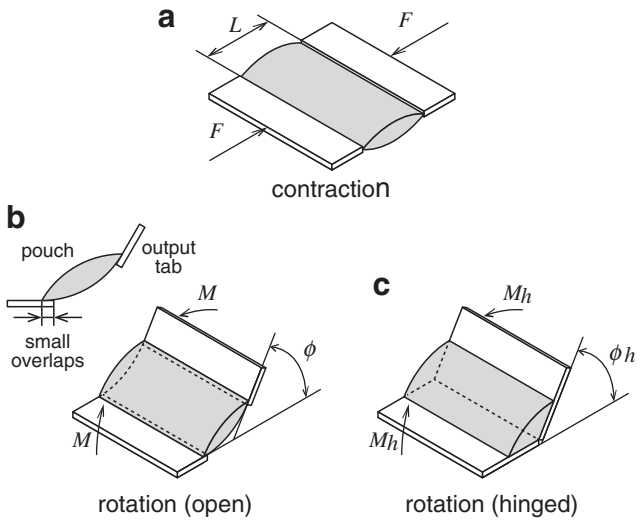

FIG. 3. Actions of the pouches: **(a)** contraction; **(b)** rotation, assuming that output tabs are tangent with the curve of the membrane on one side; and **(c)** rotation with a hinged mechanical structure.

stored in the membrane. We also assume that the width of the pouch D remains constant as it is inflated and the side surfaces are ignorable.

Assuming that the surfaces of the pouch are cylindrical, we obtain Equations (1) and (2):

$$L_0 = 2r\theta \tag{1}$$

$$r \sin\theta = \frac{L}{2} \tag{2}$$

where L_0 is the initial length when the pouch is flat, r is the radius of the curve of the membrane, θ is the central angle of the circular segment, and L is the length of the chord or the length of the pouch.

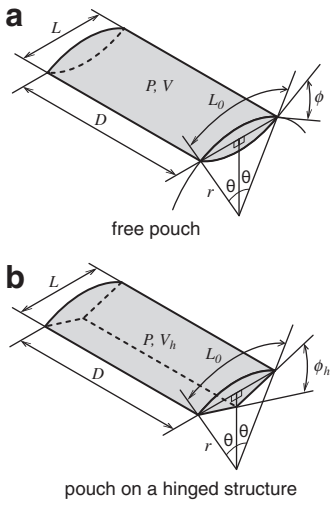

FIG. 4. Model of the single pouch: **(a)** a free pouch with cylindrical surfaces on the top and bottom, and **(b)** a pouch on a hinged joint.

From Equations (1) and (2), by eliminating the radius r, we obtain the length of the pouch; that is,

$$L(\theta) = L_0 \frac{\sin\theta}{\theta} \tag{3}$$

The above Equation (3) is applicable in both of the pouches. The volume V of the free pouch (Fig. 4a) can be derived as

$$V(\theta) = AD = \frac{{L_0}^2 D}{2}\left(\frac{\theta - \cos\theta\sin\theta}{\theta^2}\right) \tag{4}$$

where A is the cross-sectional area of the pouch and D is a width of the pouch.

The volume V_h of the pouch with hinged structure can be derived using a cross-sectional area of the pouch A_h and the width of the pouch D as follows:

$$\begin{aligned} V_h(\theta) &= A_h D \\ &= {L_0}^2 D \frac{\theta - \cos\theta\sin\theta + \sin\theta\sqrt{\theta^2 - (\sin\theta)^2}}{4\theta^2} \end{aligned} \tag{5}$$

Linear pouch motor

The work of the fluid in the pouch is transformed into tension force F in the case of a linear pouch motor. The energy conservation corresponding to a virtual translation dL becomes

$$-FDL = PdV \tag{6}$$

where F is the tension force, P is the inner pressure of the pouch, dL is the small displacement in length, and dV is the small displacement in volume.

We already have both the length and the volume [Eqs. (3) and (5)] of the pouch as a function of the parameter θ. We obtain the following result:

$$F(\theta) = -P\frac{dV}{dL} = -P\frac{dv/d\theta}{dL/d\theta} \tag{7}$$

$$F(\theta) = L_0 DP\frac{\cos\theta}{\theta} \tag{8}$$

Now we introduce a strain L_e as the ratio of total deformation to the initial length:

$$L_e = \frac{L_0 - L}{L_0} = 1 - \frac{\sin\theta}{\theta} \tag{9}$$

The theoretical maximum contraction ratio of the linear pouch motor is $L_e(\pi/2) = \frac{\pi-2}{\pi} \approx 0.363$ (36.3%). The maximum force output is observed when $L = L_0$. When $\theta \to 0$, Equation (7) says $F \to \infty$. In reality, the linear pouch motor has finite maximum output force because material can stretch by the pressure and the tension force.

Angular pouch motor

Open structure (ideal). We consider an ideal model of the angular pouch motor based on the free pouch model (Figs. 3b and 4a) in which the overlaps between the pouch and output tabs are sufficiently small. The work of the fluid in the pouch is transformed into moment (torque) M. The energy conservation corresponding to a virtual rotation $d\phi$ becomes

$$Md\phi = PdV \tag{10}$$

The output angle φ is a function of θ; that is,

$$\phi(\theta) = 2\theta \tag{11}$$

We obtain the following result:

$$M(\theta) = P\frac{dV}{d\phi} = P\frac{dV/d\theta}{d\phi/d\theta} \tag{12}$$

$$M(\theta) = {L_0}^2 DP\frac{\cos\theta(\sin\theta - \theta\cos\theta)}{2\theta^3} \tag{13}$$

The theoretical maximum range of motion of the angular pouch motor with open structure is zero to π rad (180°). The maximum moment is observed when $\phi = 0$. In practical use, because of the small overlaps between rigid output tabs and edges of the pouch (Fig. 3b), measured maximum range of motion might be less than 180°.

Hinged structure. The angular pouch motor with open structure is suitable for small-load applications such as animated origami structure. However, the open edges of the tabs will dig into the pouch with overload. By adding a hinged structure, the deformation of the pouch is efficiently transformed into the angular motion without undesired pouch deformation. Moreover, the hinge can support shear and twist force that cannot be tolerated by only the flexible pouch. On the other hand, hinged angular pouch motor has limited maximum range of motion.

The pouch motor with hinged structure (Figs. 3c and 4b) has the output angle ϕ_h, which is a function of θ. The following equation can be derived from the geometric relationships:

$$\phi_h = \cos^{-1}\left(\frac{2(\sin\theta)^2}{\theta^2} - 1\right) = 2\cos^{-1}\left(\frac{\sin\theta}{\theta}\right) \tag{14}$$

We obtain the following result for the moment M_h:

$$M_h(\theta) = P\frac{dV_h}{d\phi_h} = P\frac{dV_h/d\theta}{d\phi_h/d\theta} \tag{15}$$

$$\begin{aligned} M_h(\theta) = \frac{{L_0}^2 DP}{8\theta^2}\Big(&-1 + \theta^2 + \cos 2\theta \\ &- \sqrt{2}\cos\theta\sqrt{-1 + 2\theta^2 + \cos 2\theta}\Big) \end{aligned} \tag{16}$$

The theoretical maximum range of motion of the angular pouch motor with hinged structure is zero to 1.63 rad (95.3°). The maximum moment is observed when $\phi_h = 0$ and $M_h(0) > M(0)$.

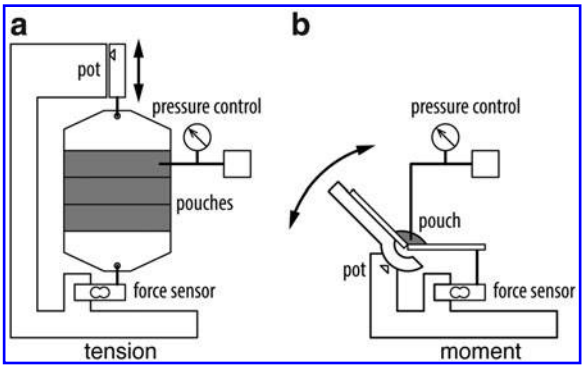

FIG. 5. The experimental setup for **(a)** tension and **(b)** moment measurements. Supply pressure of the pouch is feedback controlled during the testing.

Properties of the linear actuators

We tested a linear pouch motor with three series pouches (Fig. 5a). The test sample is made from a polyethylene sheet with a thickness of 0.102 mm (4mil). The pouches are manually fabricated by using a line heat sealer. Each pouch has the effective width $D=0.075$ m and the initial length $L_0=0.025$ m. The measurement of the tension force is a quasi-static process, which starts shortening from $L=L_0$ and returns to the initial length at a velocity of about 25 mm/min. The inner pressure of the pouch is kept constant by feedback control during the experiments.

The theoretical curves are the parametric plot of the Equations (8) and (9) for $0<\theta\leq\pi/2$. Force F is a monotonically decreasing function of the strain L_e in any pressure and is slightly concave up.

The comparison of the theoretical and the measured force–length properties is shown in Figure 6. The recordings are low-pass filtered with a cutoff frequency of 0.4 Hz. The measured data trend similarly to the model. The measured maximum stroke and force of the linear pouch motor are about 28% of the initial length and 100 N (10 kgf), respectively, in 40 kPa. This performance is comparable to McKibben artificial muscle.

We observed agreement between the theoretical curve and the measured data in small working pressures under 10 kPa. Because of the elasticity of the sheet material, the inextensible assumption is no longer valid in high working pressure over 40 kPa. This results in a relatively large error in high pressure. Even a fully loosened pouch motor (tension equal to zero) cannot reach the theoretical maximum contraction ratio. The elastic deformation also affects the maximum tension force. In the initial length ($L=L_0$), the pressured pouch cannot remain flat and has some curvature. Thus, the measured data have limited tension force in small strain. Another factor is the incomplete inflation in large contraction due to the 2D-based design of the pouch.

Properties of the angular actuators

We tested an angular pouch motor with hinged structure (Fig. 5b). The test sample is made from a polyethylene sheet with a thickness of 0.049 mm. We use a single pouch that has the effective width $D=0.075$ m, and the initial length $L_0=0.025$ m. The pouch is fabricated by using the heat drawing machine. The measurement of the moment is a quasi-static process that starts bending from $\varphi_h=0$ until $M_h=0$ and then returns to the initial angle.

The theoretical curves are the parametric plot of the Equations (14) and (16) for $0<\theta\leq\pi/2$. The moment M_h is a monotonically decreasing function of the angle φ_h in any pressure.

The comparison between theoretical and measured moment–angle properties is shown in Figure 7. The recordings are low-pass filtered with a cutoff frequency of 0.4 Hz. The

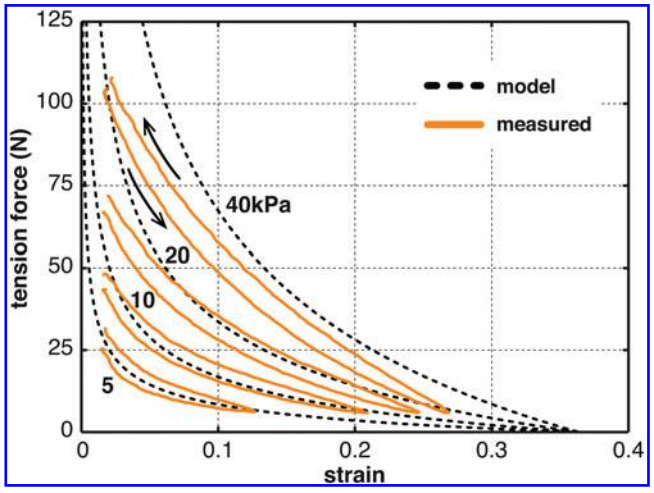

FIG. 6. The force–length relationship of the linear pouch motor at various pressures. Solid lines show measured data, and dotted lines show the corresponding theoretical curves. The arrows indicate outward and return of the hysteresis curve. The horizontal axis shows the ratio of the total deformation to the initial length L_0. Color images available online at www.liebertpub.com/soro

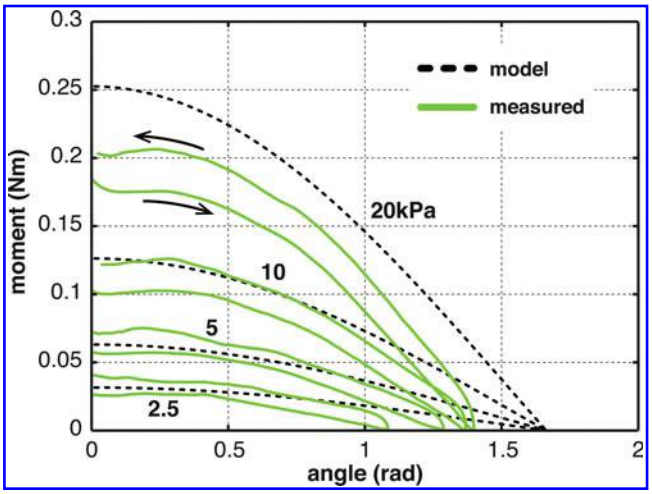

FIG. 7. The moment–angle relationship of the angular pouch motor with hinged structure at various pressure. Solid lines show measured data, and dotted lines show the corresponding theoretical curves. The arrows indicate outward and return of the hysteresis curve. Color images available online at www.liebertpub.com/soro

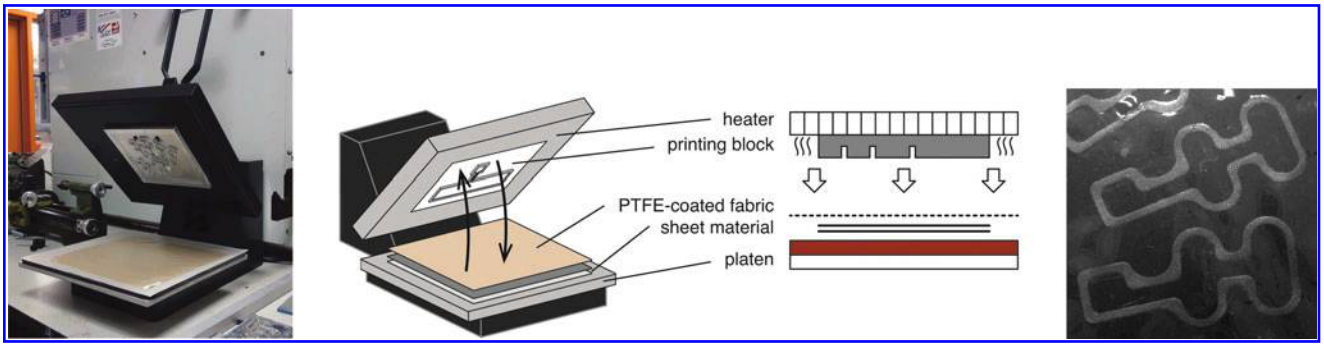

FIG. 8. The heat stamping system and a sample of the fabricated pouch. Color images available online at www.liebertpub.com/soro

measured maximum angle and moment of the hinged angular pouch motor are about 80° and 0.2 Nm, respectively, in 20 kPa.

We observed agreement between the theoretical curve and the measured data in small working pressures under 5 kPa. Because the inflated pouch does not have a perfect cylindrical shape, side wrinkles could have prevented the inflation and rotation at larger angle positions. In addition, the elastic elongation of the membrane interferes with both maximum moment and range of motion at large pressures.

Fabrication Methods

Overview

Pouch motors can be made of thermoplastic films. Two sheets of plastic film are stacked together and thermally bonded by applying heat and pressure along the line of the bonding to form a pouch. A similar thermal bonding method is used to seal bubble wraps and plastic food storage bags. To bond the two sheets along the desired shape, we develop two automated fabrication methods: heat stamping and heat drawing.

Heat stamping involves a lengthy workflow but allows for rapid manufacturing. First, a stamp (or printing block) must be made and attached to the heat press machine. Although machining a stamp takes longer process, once the stamp is ready, it is easy to duplicate the same design quickly with constant quality, thus making this method suitable for mass fabrication.

The workflow for heat drawing, in contrast, is flexible and programmable but prolongs manufacturing time. Once the pouch design is made, a heat pen attached on a three-axis CNC stage draws the outline of the design. The heat drawing method is suitable for on-demand prototyping in a small quantity.

Fabrication by stamping

The heat stamping machine consists of a heat press with a die mounted on its top plate (Fig. 8). Two layers of thermoplastic films and a nonsticky film on the top are loaded onto the machine table. We used a polytetrafluoroethylene (PTFE)-coated glass fiber fabric to prevent plastic films from sticking to the die. After heating up the die to the desired temperature, the die is pressed onto the film layers and held for a short period of time. Then the films can be taken out for cooling. Finally, pouch motors can be cut from the films. The quality of pouch motors made with thermal bonding is related to multiple parameters (Table 1).

In our process, we use 0.102-mm (4 mil)-thick vinyl films covered with a layer of 0.127-mm (5 mil)-thick PTFE-coated glass fiber fabric as the release sheet to prevent vinyl film melt onto the die. Line width on the die is 1.6 mm. We need a temperature of around 245°C when pressing the die onto the films for about 5 s.

Fabrication by drawing

The heat drawing method uses a soldering iron that is pressed against two thermoplastic films to apply heat and pressure (Fig. 9). The position of the heated metal tip of the soldering iron is controlled by a three-axis CNC stage. Nonsticky films are stacked on top of two layers of target thermoplastic films to minimize friction between the tip and the films. These materials are held on the drawing table beneath the heated tip. The heat-drawing machine uses an elastic baseboard on the table to achieve stable contact pressure. A computer interprets a line of G-code and commands the machine to move the heated tip to draw the design.

The width of the bonding lines by drawing has uniform width as shown in the sample (Fig. 9). In contrast, the

Table 1. Heat Bonding Parameters

	Bonding method	
	Heat stamping	*Heat drawing*
Line width	Die pattern width	Tip diameter, drawing force, and base board rigidity
Temperature	Die temperature	Pen-tip temperature
Process time	Stamping time	Drawing speed
Sealing force	Stamping pressure	Drawing force
Common parameters	Thickness and type of thermoplastic Thickness and type of nonstick sheet	

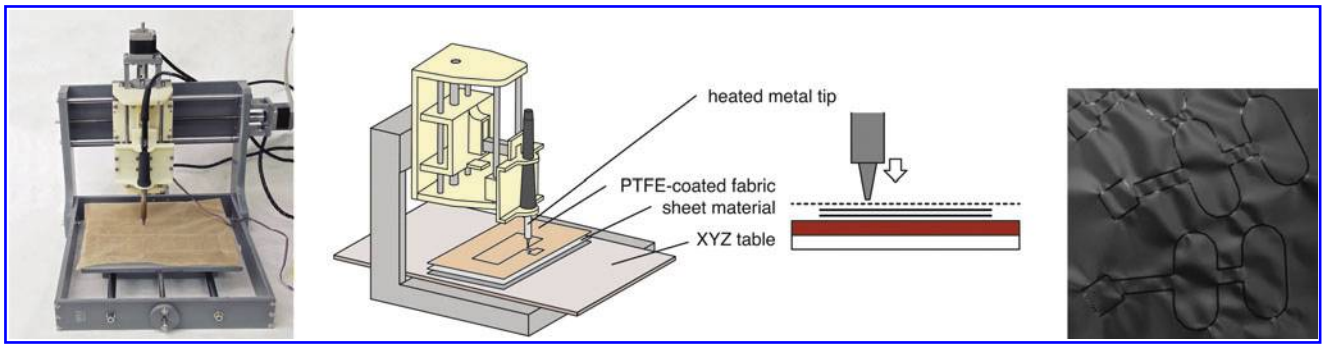

FIG. 9. The heat drawing system and a sample of the fabricated pouch. Color images available online at www.liebertpub.com/soro

stamped lines determined by the die design have more complexity. The machine also can draw a thick line by adding offset parallel lines or drawing serpentine pattern.

The quality of heat bonding is determined by multiple parameters (Table 1). We use thermoplastic films from 0.05 to 0.2-mm (2–8 mil)-thick and 0.076-mm (3 mil)-thick PTFE-coated glass fiber fabric for nonstick and low-friction drawing. We use 375 mm/min as the limiting speed of the drawing, and set the heated metal tip temperature to 357°C. The resulting drawing force to make workable pouches is about 6.9 N.

Automated Design with Pouch Motors

Overview

The pouch motor is not only printable but also it is suitable for automated design. The pouch motor design can be reduced to 2D graphics and not suffered from complicated 3D geometric constraints. The users can benefit from computer-based optimization and simulation. Moreover, the automated design can provide an opportunity for nonprofessional people to design robot systems. This section describes the design algorithm for software developers.

The design algorithm for robots with pouch motors compiles a 3D origami design (a folded state of a paper structure encoded with a crease pattern and folded angles) or a 3D polygon mesh into a design for pouch motor robots. This automated design process has three parts:

1. Creating unfolded 2D structure
2. Positioning pouch motors and routing air channels
3. Generating paths for CNC fabrication

Creating a 2D pattern from a 3D model

Several algorithms exist to unfold 3D meshes or origami designs.[26–28] We modified the algorithm for self-folding sheets[29] to output a 2D unfolded structure for later process. We transform the 3D model as a graph and unfold it using Prim's algorithm (a minimum spanning tree algorithm).[30] As the algorithm unfolds the 3D model, it maintains the relationship between the vertexes of the unfolded 2D pattern and the 3D model.

Positioning pouches and routing

Once a 2D pattern has been developed, users can indicate groups of actuated folds. Our system places pouches on the fold pattern and routes air channels to allow groups of pouches to be actuated simultaneously. The current system is exclusive to angular pouch motors attached on folds. We use the following steps, depicted in Figure 10:

Input. The user provides a fold pattern $G=(B, F)$, where $B \subset \mathbb{R}^2$ is the boundary of the unfolding and F is a list of

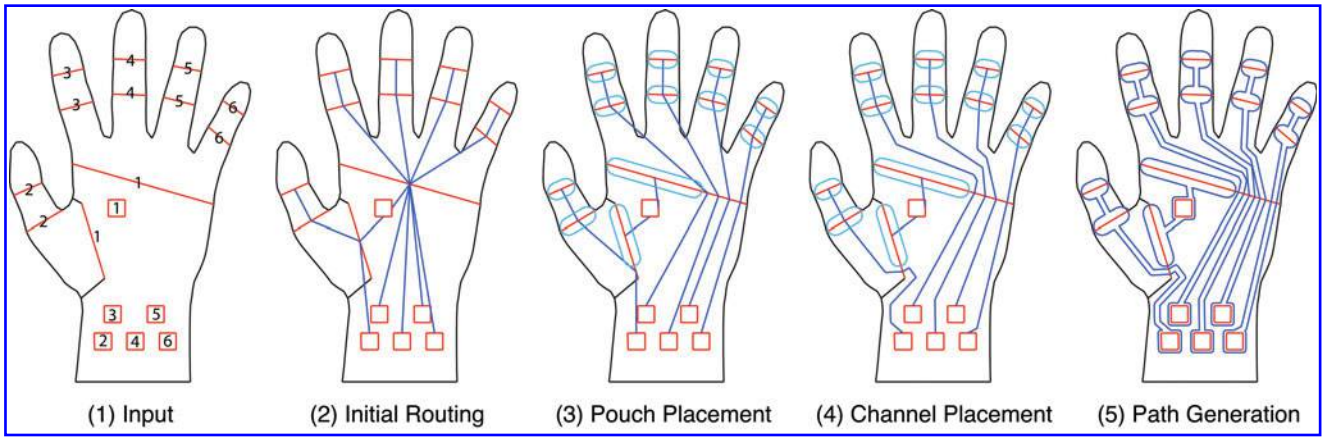

FIG. 10. Procedure for placing pouches and routing air channels on a fold pattern. Color images available online at www.liebertpub.com/soro

folds f_i in the fold pattern. Together, the boundary and the folds divide the fold pattern into *faces*. The user inputs a list A of n_p face ids, which are where the input ports are located, as well as a mapping $s : F \rightarrow \{0, 1, \cdots, n_p\}$, which indicates which folds are associated with each input port. A fold f_i with $s(f_i) = 0$ is not actuated and does not correspond to any port. Figure 10(1) illustrates the input. Folds are shown in red, and cuts are shown in black. Folds that are labeled with the same number are to be actuated together. For example, the two joints in the thumb are actuated together, but they move independently of all other fingers. The squares at the wrist and in the palm are the input ports.

Initial routing (Algorithm 1, lines 2–8). Using these inputs, our system constructs a graph $G = (F, E)$ of the available space, where $E = \{(f_i, f_j) | f_i \text{ and } f_j \text{ bound the same face}\}$. Each edge $(f_i, f_j) \in E$ has a weight $w(f_i, f_j)$, which is the shortest Euclidean distance between the midpoints of folds f_i and f_j in the unfolding. Then, for each input port a_k, we use Prim's algorithm[30] to find the subgraph of G with minimum total weight that spans all the folds in the group (i.e., all folds f_i such that $s(f_i) = k$). The blue lines in Figure 10(2) show the result of this step. For all four fingers and the thumb, the distal joint connects through the proximal joint and across the palm to the input port at the wrist. On the other hand, for the palm, both joints connect directly to the input port.

Algorithm 1: Initial Rounting

Input: A fold pattern $G = (B, F)$, a list A of n_a of face ids a_k corresponding to input ports, a mapping $s : F \rightarrow \{0, 1, 2, \cdots, n_a\}$ of folds to ports, a width d_c for the channels, and width d_p for the pouches

```
// Input Ports
```
1 $A_F \leftarrow \bigcup_{a_k \in A} \{x \in \mathbb{R}^2 | x \text{ in face } a_k\}$;
```
// Initial Routing
```
2 $E \leftarrow \{(f_i, f_j) | f_i, f_j$ are edges of the same face in the unfolding$\}$;
3 **for** *each* $(f_i, f_j) \in E$ **do**
4 $\quad w(f_i, f_j) \leftarrow$ Euclidean distance between midpoints of f_i and f_j;
5 **end**
6 **for** $k \leftarrow 1$ *to* n_a **do**
7 $\quad T_k \leftarrow \text{PRIM}((F, E), w, s, k)$
8 **end**

Pouch placement (Algorithm 2, lines 1–12). For each fold in the input design, our system next spaces out the channels that cross the fold. If the fold is actuated, it calculates the maximum length of the pouch l_i that will still allow other air channels to cross the fold. In addition, pouches of width d_p are drawn. In Figure 10(3), pouches for both joints in the palm must be shorter than the length of the fold to allow air channels to pass. On the other hand, pouches in the finger joints can be as long as the folds.

Algorithm 2: Pouch and Channel Placement

```
// Pouch Placement
```
1 $P \leftarrow \emptyset$;
2 **for** *each* $f_i \in F$ **do**
3 $\quad n_i \leftarrow$ number of subgraphs T_k that contain f_i;
4 $\quad$ **if** $s(f_i) \neq 0$ *AND* f_i *does not bound face* $a_{s(f_i)}$ **then**
```
// actuated f_i needs a pouch
```
5 $\quad\quad l_i \leftarrow \text{length}(f_i) - d_c n_i - d_p$;
6 $\quad\quad$ For all k s.t. $f_i \in T_k$, set v_i^k spaced along f_i, with distance $l_i/2$ between $v_i^{s(f_i)}$ and its neighbors and the rest evenly spaced;
7 $\quad\quad P \leftarrow P \cup \left\{x \in f_i | \text{dist}\left(x, v_i^{s(f_i)}\right) \leq l_i/2\right\}$;
```
// pouch centerline
```
8 $\quad$ **else**
9 $\quad\quad$ For all k s.t. $f_i \in T_k$, set v_i^k spaced evenly along f_i;
10 $\quad$ **end**
11 **end**
12 $P \leftarrow \{x \in \mathbb{R}^2 | \text{dist}(x, P) < d_p\}$; `// pouch area`
13 **for** $k \leftarrow 1$ *to* n_a **do**
```
// Channel Placement
```
14 $\quad T_k^e \leftarrow \emptyset$;
15 $\quad$ **for** *each edge* (f_i, f_j) *in* T_k **do**
16 $\quad\quad$ Add to T_k^e a path from v_i^k to v_j^k that does not intersect $B \cup A_F \cup \bigcup_{m=1}^{k-1} T_m^e$;
17 $\quad$ **end**
```
// Path Generation
```
18 $\quad T_k^e \leftarrow \{x \in \mathbb{R}^2 | \text{dist}(x, T_k^e) < d_c\}$;
```
// channel area
```
19 **end**
```
// Combined air channels
```
20 $C \leftarrow P \cup A_F \cup \bigcup_{k=1}^{n_a} T_k^e$;
21 **return** boundary of C;

Channel placement (Algorithm 2, lines 14–17). Each channel is drawn so that it avoids crossing over cut lines or colliding with pouches and other channels in the design. Initially, every edge in the tree T_k is converted into a straight line segment. Then, we iteratively check over the segments of the embedded tree $T_k{}^e$, adding vertices and segments whenever an intersection is found. We take a greedy approach, where the channels for one entire actuation group are determined before proceeding to the next group. In Figure 10(4), the air channel leading to the palm was adjusted to curve around the pouch in the palm and the cut line below it.

Path generation (Algorithm 2, lines 18–21). Finally, the routes for the air channels are thickened to width d_c and outlines for the combined air channels (including pouches, input ports, and routes) are produced [Fig. 10(5)]. The drawing is saved in DXF format for fabrication.

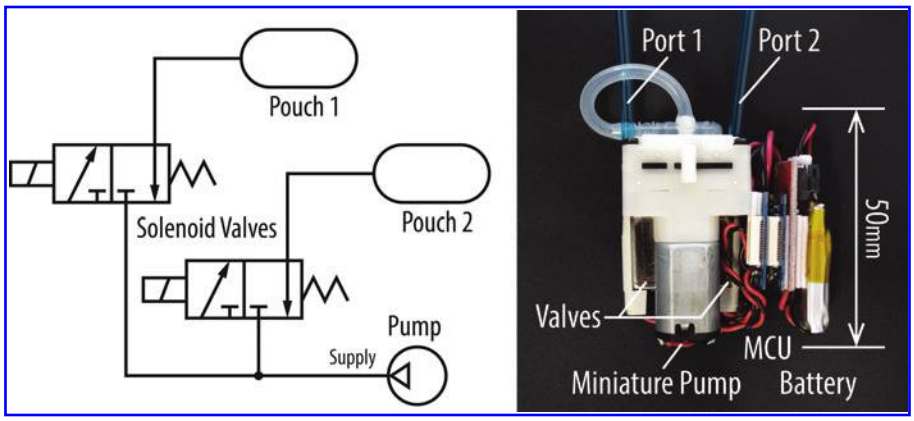

FIG. 11. Left: the pneumatic circuit for controlling two pouches individually. Right: the implemented portable miniature pneumatic control system that is used for the robotic hand. Color images available online at www.liebertpub.com/soro

Digital fabrication

With the DXF file, we can generate tool paths to make a die for heat stamping or to control a heat drawing machine. We generated a computer numerical control program (G-code) with CAM software for the computer-controlled fabrication.

Because of the unique setup of heat drawing machine, a few calibration steps are necessary for the z axis to adjust drawing forces. Following the calibration, codes are loaded to the machine and pouches can be printed.

Robotic Application

Miniature pneumatic control system

We developed a portable pneumatic control system that consists of a miniature pump, tiny solenoid valves, battery, and microcontroller unit (Fig. 11).

The system can share one pump for multiple pouch motors. Two 2-way 3-port valves are needed per pouch to achieve the three states: supply, exhaust, and keep air. For the binary functions (supply/exhaust), the control system requires only one solenoid valve per pouch.

Robotic hand

We developed several versions of a life-sized robotic hand (Fig. 12). The robotic hand can perform hand gestures, and grasp a paper cup and a foam ball by supplying air through the ports. The compliant joints enable the hand to adapt to an object with irregular shape such as human hand. A hand made of paper board structure, with weight of 20 g, experienced delamination due to the tension of the pouch. A hand made of acrylic board structure, with weight of 80 g, has stable hinged structure. Robotic hands are fabricated by using both heat stamping and heat drawing method. Stamping the actuator layer takes about 10 s, and heat drawing takes about 10 min. We found no significant difference in performance of the actuators with two fabrication methods in fixed pattern. The

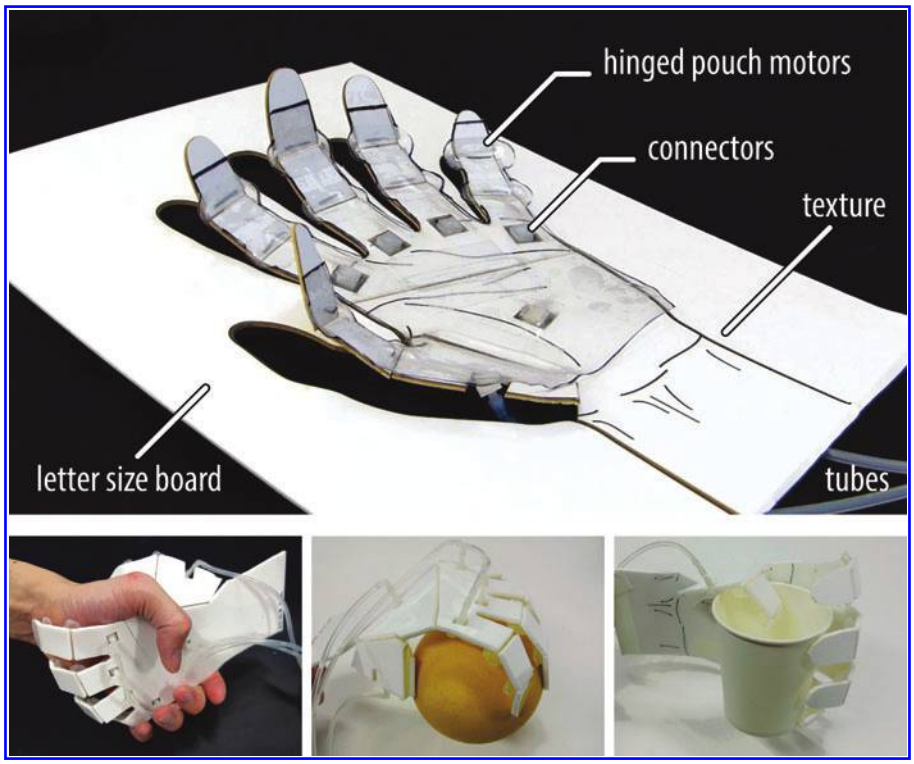

FIG. 12. The planar printable robotic hand driven by the hinged pouch motors fabricated on a letter size board. The hand can grip human hand, grasp a foam ball, and hold a paper cup. Color images available online at www.liebertpub.com/soro

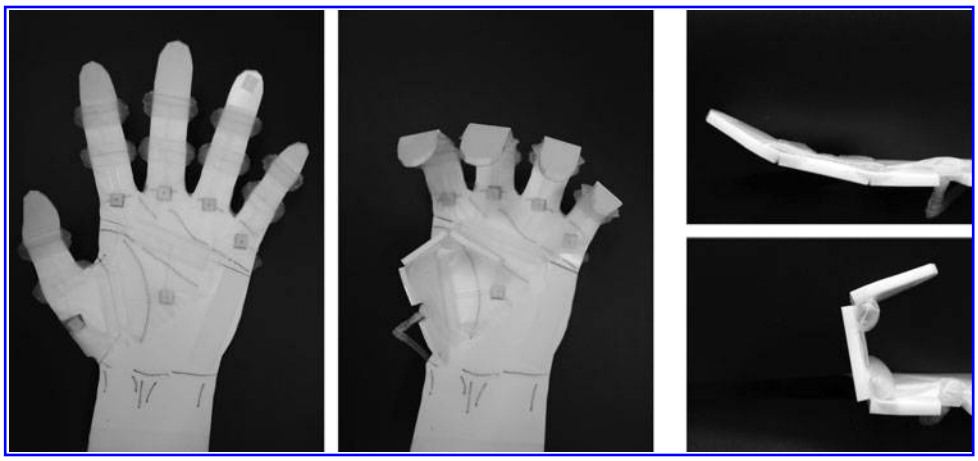

FIG. 13. The range of motion of the robotic hand. Left: overall view. Right: side view of the thumb extension and flexion.

aspect ratio of the pouch should be 1:2 or longer along the actuated edge to obtain uniform cylindrical shape when inflated. We also observed that the pouch that is slightly longer than the length of the actuated edge could achieve larger torque without peel off from the structure.

The miniature pneumatic control system can control two groups of air channels. Tubing connectors are attached on the actuator layer by double-sided tape. We put pneumatic tubes for all the fingers except the thumb together and link tubes for thumb and palm joints together. Fully extended fingers can produce the force about 0.6 N on the fingertip with the air pressure of 40 kPa. The maximum range of motion for each joint is about 80° (Fig. 13). The speed of the extension and flexion of the finger is up to 1 Hz with the portable pneumatic control system. We conducted both programmed sequence of motion and interactive movements based on the push buttons.

We have tested our design algorithm on several configurations of actuators and input ports for the robotic hand (Fig. 14). All those samples are fabricated by using the heat drawing method. Air channels are arranged so that they do not cross over each other or over cuts in the fold pattern. Comparing results show that the pouch lengths are adjusted to accommodate air channels. Other examples show different actuator groups; air channels branch to simultaneously actuate multiple fingers.

Conclusions

We propose a printable soft actuator that we term a ''pouch motor.'' This planar pneumatically driven actuator allows a

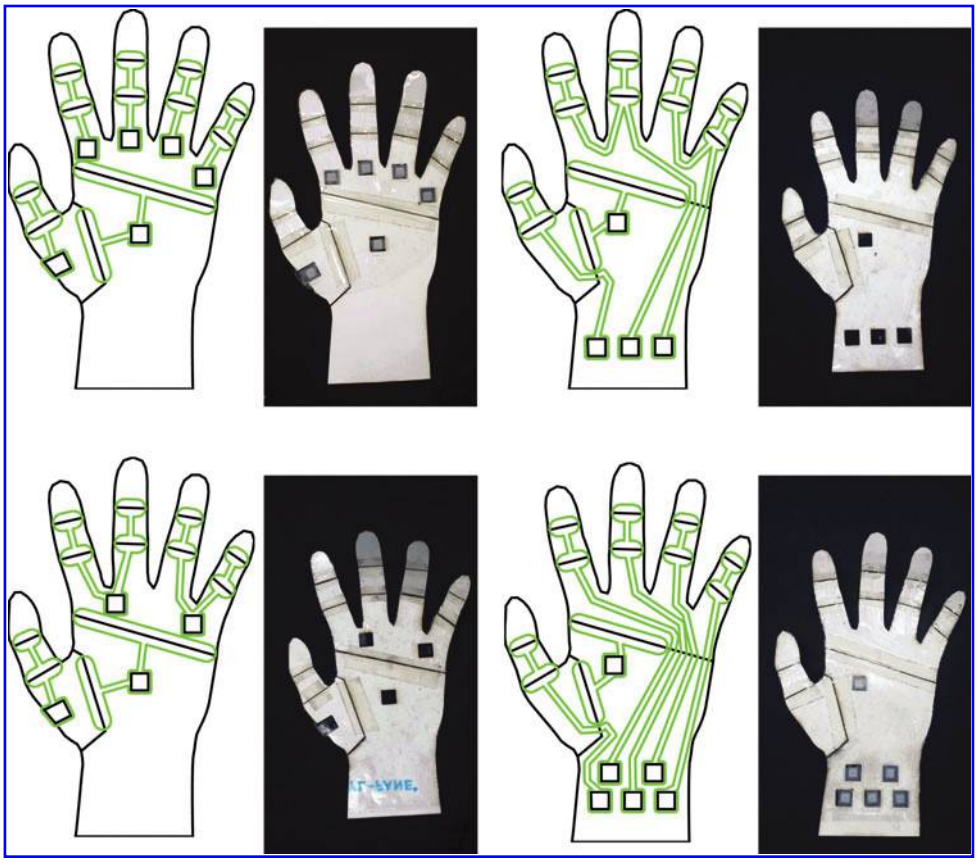

FIG. 14. The computer-generated robotic hands design with different grouping of pouches. These designs are fabricated by the heat drawing method. Color images available online at www.liebertpub.com/soro

streamlined design and fabrication process. We provide both a semiautomated design process of the pouch motors with air channels, and a fabrication method based on heat bonding. The pouch motors can be scaled up or down using different materials and fabrication methods. The mathematical models of the linear pouch motor and angular pouch motor can predict measured values. We demonstrate the proposed design method with a planar robotic hand with 12 pouch motors. The system can provide a variety of air channel arrangements corresponding to the different user inputs. Future work may encompass more complicated 3D structures and optimized design methods. Integration of a sensing layer with feedback control is the next step toward developing fully printable robots.

Acknowledgments

This work was funded in part by National Science Foundation Grant Nos. 1240383 and 1138967. Support was also provided in part by the Department of Defense under the National Defense Science and Engineering Graduate Fellowship Program. We are grateful for this support.

Author Disclosure Statement

No competing financial interests exist.

References

1. Onal CD, Wood RJ, Rus D. Towards printable robotics: origami-inspired planar fabrication of three-dimensional mechanisms. In: Proceedings of the IEEE International Conference on Robotics and Automation (ICRA), 2011, pp. 4608–4613.
2. Bailey SA, Cham JG, Cutkosky MR, Full RJ. Biomimetic robotic mechanisms via shape deposition manufacturing. In: Proceedings of the 9th International Symposium of Robotics Research, 1999, pp. 321–327.
3. Dollar AM, Howe RD. A robust compliant grasper via shape deposition manufacturing. IEEE/ASME Trans Mechatron 2006;11:154–161.
4. Wood RJ, Avadhanula S, Menon M, Fearing RS. Microrobotics using composite materials: the micromechanical flying insect thorax. In: Proceedings of the IEEE International Conference on Robotics and Automation (ICRA), 2003, pp. 1842–1849.
5. Hoover AM, Fearing RS. Fast scale prototyping for folded millirobots. In: Proceedings of the IEEE International Conference on Robotics and Automation (ICRA), 2008, pp. 886–892.
6. Felton SM, Tolley MT, Shin B, Onal CD, Demaine ED, Rus D, Wood RJ. Self-folding with shape memory composites. Soft Matter 2013;9:7688–7694.
7. Murata S, Yoshida E, Kamimura A, Kurokawa H, Tomita K, Kokaji S. M-TRAN: self-reconfigurable modular robotic system. IEEE/ASME Trans Mechatron 2002;7:431–441.
8. Hawkes E, An B, Benbernou NM, Tanaka H, Kim S, Demaine ED, Rus D, Wood RJ. Programmable matter by folding. Proc Natl Acad Sci USA 2010;107:12441–12445.
9. Knaian AN, Cheung KC, Lobovsky MB, Oines AJ, Schmidt-Neilsen P, Gershenfeld NA. The milli-motein: a self-folding chain of programmable matter with a one centimeter module pitch. In: Proceedings of the IEEE/RSJ International Conference on Intelligent Robots and Systems (IROS), 2012, pp. 1447–1453.
10. Kawahara Y, Hodges S, Cook BS, Zhang C, Abowd GD. Instant inkjet circuits. In: Proceedings of the ACM International Joint Conference on Pervasive and Ubiquitous Computing (UbiComp), 2013, pp. 363–372.
11. Sun K, Wei T-S, Ahn BY, Seo JY, Dillon SJ, Lewis JA. 3D printing of interdigitated Li-ion microbattery architectures. Adv Mater 2013;25:4539–4543.
12. Willis K, Brockmeyer E, Hudson S, Poupyrev I. Printed optics: 3D printing of embedded optical elements for interactive devices. In: Proceedings of the ACM Symposium on User Interface Software and Technology (UIST), 2012, pp. 589–598.
13. Egawa S, Niino T, Higuchi T. Film actuators: planar, electrostatic surface-drive actuators. In: Proceedings of the IEEE International Conference on Micro Electro Mechanical Systems (MEMS), 1991, pp. 9–14.
14. Seok S, Onal CD, Cho K-J, Wood RJ, Rus D, Kim S. Meshworm: a peristaltic soft robot with antagonistic nickel titanium coil actuators. IEEE/ASME Trans Mechatron 2013;18:1485–1497.
15. Haines CS, Lima MD, Li N, Spinks GM, Foroughi J, Madden W, Kim SH, Fang S, Jung de Andrade M, Göktepe F, Göktepe O, Mirvakili SM, Naficy S, Lepró X, Oh J, Kozlov ME, Kim SJ, Xu X, Swedlove BJ, Wallace GG, Baughman RH. Artificial muscles from fishing line and sewing thread. Science 2014;343:868–872.
16. Ilievski F, Mazzeo AD, Shepherd RF, Chen X, Whitesides GM. Soft robotics for chemists. Angew Chem Int Ed 2011;50:1890–1895.
17. Martinez RV, Fish CR, Chen X, Whitesides GM. Elastomeric origami: programmable paper-elastomer composites as pneumatic actuators. Adv Funct Mater 2012;22:1376–1384.
18. De Volder M, Reynaerts D. Pneumatic and hydraulic microactuators: a review. J Micromech Microeng 2010;20:043001.
19. Kawai F, Cusin P, Konishi S. Thin flexible end-effector using pneumatic balloon actuator. In: Proceedings of the IEEE International Conference on Micro Electro Mechanical Systems, 2000, vol. 89, pp. 28–35.
20. Lu Y, Kim C-J. Characterization of balloon-jointed microfingers. In: Proceedings of the ASME International Mechanical Engineering Congress and Exposition, 2003, pp. 311–316.
21. Gorissen B, Volder MD, Greef AD, Reynaerts D. Theoretical and experimental analysis of pneumatic balloon microactuators. Sens Actuat A 2011;168:58–65.
22. Bergemann D, Lorenz B, Thallemer A. Actuating means. U.S. Patent 6,349,746, Feb. 26, 2002.
23. Daerden F, Lefeber D. The concept and design of pleated pneumatic artificial muscles. Int J Fluid Power 2001;2:41–50.
24. Niiyama R, Rus D, Kim S. Pouch motors: printable/inflatable soft actuators for robotics. In: Proceedings of the IEEE International Conference on Robotics and Automation (ICRA), 2014, pp. 6332–6337.
25. Park Y-L, Santos J, Galloway KG, Goldfield EC, Wood RJ. A soft wearable robotic device for active knee motions using flat pneumatic artificial muscles. In: Proceedings of the IEEE International Conference on Robotics and Automation (ICRA), 2014, pp. 4805–4810.
26. Tachi T. Origamizing polyhedral surfaces. IEEE Trans Vis Comput Graph 2010;16:298–311.
27. Takahashi S, Wu H-Y, Saw S, Lin C-C, Yen H-C. Optimized topological surgery for unfolding 3D meshes. Comput Graph Forum 2011;30:2077–2086.

28. Tachi T. Simulation of rigid origami. In: Proceedings of the Origami4: International Conference on Origami in Science, Mathematics and Education (OSME), 2009, pp. 175–187.
29. An B, Miyashita S, Tolley MT, Aukes DM, Meeker L, Demaine ED, Demaine ML, Wood RJ, Rus D. An end-to-end approach to making self-folded 3D surface shapes by uniform heating. IEEE International Conference on Robotics and Automation (ICRA), 2014.
30. Prim RC. Shortest connection networks and some generalizations. Bell Syst Tech J 1957;36:1389–1401.

Address correspondence to:
Ryuma Niiyama
Department of Mechano-Informatics
School of Information Science and Technology
University of Tokyo
Eng. Bld. 2, Room 82D4, 7-3-1 Hongo, Bunkyoku
Tokyo 113-0033
Japan

E-mail: niiyama@isi.imi.i.u-tokyo.ac.jp

This article has been cited by:

1. Chen Feifei, Wang Michael Yu, Zhu Jian, Zhang Y.F.. 2016. Interactions Between Dielectric Elastomer Actuators and Soft Bodies. *Soft Robotics* **3**:4, 161-169. [Abstract] [Full Text HTML] [Full Text PDF] [Full Text PDF with Links]
2. Lindsey Hines, Kirstin Petersen, Guo Zhan Lum, Metin Sitti. 2016. Soft Actuators for Small-Scale Robotics. *Advanced Materials* 1603483. [CrossRef]
3. Allan Joshua Veale, Sheng Quan Xie, Iain Alexander Anderson. 2016. Modeling the Peano fluidic muscle and the effects of its material properties on its static and dynamic behavior. *Smart Materials and Structures* **25**:6, 065014. [CrossRef]
4. Allan Joshua Veale, Sheng Quan Xie, Iain Alexander Anderson. 2016. Characterizing the Peano fluidic muscle and the effects of its geometry properties on its behavior. *Smart Materials and Structures* **25**:6, 065013. [CrossRef]
5. Xu Sun, Samuel M. Felton, Robert J. Wood, Sangbae KimPrinting angle sensors for foldable robots 1725-1731. [CrossRef]
6. Lindsay Sanneman, Deborah Ajilo, Joseph DelPreto, Ankur Mehta, Shuhei Miyashita, Negin Abdolrahim Poorheravi, Cami Ramirez, Sehyuk Yim, Sangbae Kim, Daniela RusA Distributed Robot Garden System 6120-6127. [CrossRef]
7. Xu Sun, Samuel M. Felton, Ryuma Niiyama, Robert J. Wood, Sangbae KimSelf-folding and self-actuating robots: A pneumatic approach 3160-3165. [CrossRef]